Journal of Geodesy (2001) 74: 690–700

Journal of Geodesy

A new approach for airborne vector gravimetry using GPS/INS

J. H. Kwon, C. Jekeli

Department of Civil and Environmental Engineering and Geodetic Science, 2070 Neil Avenue, Columbus, OH 43210, USA
e-mail: kwon.28@osu.edu; jekeli.1@osu.edu

Received: 18 April 2000 / Accepted: 14 August 2000

Abstract. A new method for airborne vector gravimetry using GPS/INS has been developed and the results are presented. The new algorithm uses kinematic accelerations as updates instead of positions or velocities, and all calculations are performed in the inertial frame. Therefore, it is conceptually simpler, easier, more straightforward and computationally less expensive compared to the traditional approach in which the complex navigation equations should be integrated. Moreover, it is a unified approach for determining all three vector components, and no stochastic gravity modeling is required. This approach is based on analyzing the residuals from the Kalman filter of sensor errors, and further processing with wavenumber coefficient filterings is applied in case closely parallel tracks of data are available. An application to actual test-flight data is performed to test the validity of the new algorithm. The results yield an accuracy in the down component of about 3–4 mGal. Also, comparable results are obtained for the horizontal components with accuracies of about 6 mGal. The gravity modeling issue is discussed and alternative methods are presented, none of which improves on the original approach.

Key words: Airborne vector gravimetry – GPS – INS – Kalman filter – Wavenumber coefficient filter

1 Introduction

Measuring the Earth's gravity field is one of the most important activities in geodesy for the determination of the geoid and the prediction of dynamic orbits of satellites. In addition, many scientific and engineering disciplines need gravity information for exploration and navigation and to investigate geophysical phenomena. Although satellite technology makes it possible to determine the gravity field using satellite observations as evidenced by JGM-3 (Tapley et al. 1996) or satellite-borne instrumentation (gradiometer), the shorter-wavelength signatures are either poorly modeled or only moderately well known in the high-degree expansions, such as the global model EGM 96 (Lemoine et al. 1998); see Jekeli (1998). Therefore, airborne gravimetry plays a very important role in recovering the Earth's gravity field in the range of medium to high frequencies, which then fills the gap between the terrestrial gravity field measurements and global gravity models in the wavelengths between 1 and 100–200 km (Hein 1995).

Currently, airborne gravimetry is conducted using either sea/air gravimeters on a stabilized platform for scalar gravimetry or with an inertial navigation system (INS) for scalar or vector gravimetry. The INS is further divided into two categories, namely a local stabilized system and strapdown INS. In all cases the Global Positioning System (GPS) provides accurate kinematic acceleration, and the separation of the gravitational acceleration from the system errors is very crucial. Results from airborne gravity surveys using modified gravimeters and GPS in Greenland, Antarctica, and Switzerland show that an accuracy of 3–5 mGal and a resolution of 10 km is achievable with current technology (Brozena and Peters 1994; Forsberg and Kenyon 1994). For a local stabilized system, an ITC-2 inertial platform system was tested and showed that an accuracy of 1 mGal with resolution of 2–3 km is achievable (Salychev et al. 1994). Unlike the above two systems, there is no physically stabilized platform in the strapdown case. Instead, the inertial sensors are physically bolted to the vehicle, and the measured data in the body frame are transformed to the local-level frame computationally. The advantages of the strapdown system are its smaller size, lower cost, and greater operational flexibility (Jekeli 1995). It has been shown that the performance of the strapdown INS is comparable to that of the stabilized airborne gravimeter (Glennie et al. 2000).

Correspondence to: C. Jekeli

The traditional way of determining the gravity disturbance components using GPS/INS data is to integrate the navigation equations associated with the INS and to model the INS errors and gravity disturbances as stochastic processes (Forsberg 1987; Eissfeller and Spietz 1989; Knickmeyer 1990; Jekeli 1994; Wang 1998; Grejner-Brzezinska and Wang 1998). GPS position and/or velocity are used as updates in a Kalman filter estimation of the errors, including the gravity disturbances, and the calculations are done in the navigation frame. Moreover, this technique is limited to the estimation of the horizontal components.

Alternatively, the gravity disturbance vector can be obtained directly by differencing the GPS and INS sensed accelerations (Jekeli 1992), which is analogous to conventional airborne scalar gravimetry using gravimeters (Brozena 1991). Based on this idea, a new algorithm for vector gravimetry has been developed for strapdown INS. In this algorithm, no stochastic gravity model is necessary and all three components are estimated in a unified approach. Furthermore, all calculations are carried out in the inertial frame, which reduces the computational complexity.

In this paper, a detailed theoretical development and the results of application to real flight data are presented. In addition, the advantages and disadvantages of the new algorithm are discussed in terms of the theoretical as well as the practical point of view.

2 Model development

The fundamental equation of airborne vector gravimetry is based on Newton's second law of motion expressed in a non-rotating, freely falling coordinate frame, called the *i*-frame, which may be identified with an Earth-centered celestial (inertial) frame

$$\ddot{\mathbf{x}}^i = \mathbf{a}^i + \mathbf{g}^i \tag{1}$$

where $\ddot{\mathbf{x}}^i$ is the second time derivative of positions, namely the kinematic acceleration; $\mathbf{a}^i$ is the specific force; and $\mathbf{g}^i$ is the gravitation. A superscript on a vector refers to the frame in which its coordinates are given. The kinematic acceleration $\ddot{\mathbf{x}}^i$ can be derived from GPS three-dimensional (3-D) positions, and the specific force $\mathbf{a}^i$ can be measured by a triad of single-axis accelerometers. Denoting the observed quantities with a tilde and the errors in the observations with δ, the fundamental equation can be expressed in terms of observations as

$$\tilde{\ddot{\mathbf{x}}}^i - \delta\ddot{\mathbf{x}}^i = \tilde{\mathbf{a}}^i - \delta\mathbf{a}^i + \mathbf{g}^i \tag{2}$$

where $\tilde{\ddot{\mathbf{x}}}^i$ is the observed acceleration derived from GPS; $\tilde{\mathbf{a}}^i$ is the specific force obtained by the INS; and $\delta\ddot{\mathbf{x}}^i$, $\delta\mathbf{a}^i$ are the respective errors in GPS and INS observed accelerations. The accelerometer error $\delta\mathbf{a}^i$ can be expressed in terms of the sensor errors in the body frame (*b*-frame) and the orientation error, according to the Coriolis Law

$$\delta\mathbf{a}^i = C_b^i\delta\mathbf{a}^b + \tilde{\mathbf{a}}^i \times \boldsymbol{\Psi}^i \tag{3}$$

where C_b^i is the transformation matrix from the body (vehicle) to the inertial frame, and $\boldsymbol{\Psi}^i$ is the orientation error of the body in the inertial frame. Error (3) is a linear approximation that neglects higher-order terms in $\delta\mathbf{a}^i$ and $\boldsymbol{\Psi}^i$. Since the accelerometers and gyros have some systematic errors, these can be modeled as well. In this study, only essential systematic errors are considered for both inertial sensors, namely biases and scale factors. GPS-observed accelerations are assumed to have only white-noise errors. Although this is not strictly true due to increased noise at high frequencies arising from the numerical differentiation, we assume that sufficient smoothing has already been applied to reduce the high-frequency errors. On the other hand, the accelerations should be devoid of biases and long-term trends, such as resulting from tropospheric and ionospheric delays. All three sensors presumably generate white noise, and we have

$$\delta\mathbf{a}^b = \mathbf{b}_a + \mathrm{diag}(\mathbf{a}^b)\boldsymbol{\kappa}_a + \boldsymbol{\varepsilon}_a \tag{4}$$

$$\delta\boldsymbol{\omega}_{ib}^b = \mathbf{b}_g + \mathrm{diag}(\boldsymbol{\omega}_{ib}^b)\boldsymbol{\kappa}_g + \boldsymbol{\varepsilon}_g \tag{5}$$

$$\delta\ddot{\mathbf{x}}^i = \boldsymbol{\varepsilon}_G \tag{6}$$

where $\boldsymbol{\varepsilon}_g \sim \mathrm{N}(\mathbf{0}, D_g)$, $\boldsymbol{\varepsilon}_a \sim \mathrm{N}(\mathbf{0}, D_a)$, and $\boldsymbol{\varepsilon}_G \sim \mathrm{N}(\mathbf{0}, D_G)$ are zero-mean, Gaussian, white-noise processes with indicated dispersion matrices. Subscripts on the vectors in Eqs. (4)–(6) provide additional specialization. For example, in Eq. (5), $\boldsymbol{\omega}_{ib}^b$ is the angular rate of the body frame with respect to the *i*-frame, expressed in *b*-frame coordinates. The biases, $\mathbf{b}_a$ for the accelerations and $\mathbf{b}_g$ for the gyros, and corresponding scale factors $\boldsymbol{\kappa}_a$, $\boldsymbol{\kappa}_g$, can be modeled as random constants

$$\dot{\mathbf{b}}_a = \mathbf{0}, \quad \dot{\boldsymbol{\kappa}}_a = \mathbf{0}, \quad \dot{\mathbf{b}}_g = \mathbf{0}, \quad \dot{\boldsymbol{\kappa}}_g = \mathbf{0} \tag{7}$$

The dynamics of the orientation error are given by

$$\begin{aligned}\dot{\boldsymbol{\Psi}}^i &= -C_b^i\delta\boldsymbol{\omega}_{ib}^b \\ &= -C_b^i\mathbf{b}_g - C_b^i\mathrm{diag}(\boldsymbol{\omega}_{ib}^b)\boldsymbol{\kappa}_g - C_b^i\boldsymbol{\varepsilon}_g\end{aligned} \tag{8}$$

where Eq. (5) is used. Combining Eqs. (7) and (8), we can set up the system model expressed by a set of linear, first-order, differential equations in terms of the INS system error parameters as well as orientation errors

$$\begin{aligned}\begin{bmatrix}\dot{\mathbf{b}}_a\\ \dot{\mathbf{b}}_g\\ \dot{\boldsymbol{\kappa}}_a\\ \dot{\boldsymbol{\kappa}}_g\\ \dot{\boldsymbol{\Psi}}^i\end{bmatrix} &= \begin{bmatrix}0 & 0 & 0 & 0 & 0\\ 0 & 0 & 0 & 0 & 0\\ 0 & 0 & 0 & 0 & 0\\ 0 & 0 & 0 & 0 & 0\\ 0 & -C_b^i & 0 & -C_b^i\mathrm{diag}(\boldsymbol{\omega}_{ib}^b) & 0\end{bmatrix}\begin{bmatrix}\mathbf{b}_a\\ \mathbf{b}_g\\ \boldsymbol{\kappa}_a\\ \boldsymbol{\kappa}_g\\ \boldsymbol{\Psi}^i\end{bmatrix}\\ &\quad + \begin{bmatrix}0 & 0 & 0 & 0 & 0\\ 0 & 0 & 0 & 0 & 0\\ 0 & 0 & 0 & 0 & 0\\ 0 & 0 & 0 & 0 & 0\\ 0 & 0 & 0 & 0 & -C_b^i\end{bmatrix}\begin{bmatrix}0\\ 0\\ 0\\ 0\\ \boldsymbol{\varepsilon}_g\end{bmatrix}\\ &= F\mathbf{s} + G\mathbf{w}\end{aligned} \tag{9}$$

which implicitly defines the state vector, $\mathbf{s}$, the noise vector, $\mathbf{w}$, and corresponding coefficient matrices, F and G.

The external observations are a combination of kinematic acceleration calculated from GPS positions and normal gravity. The corresponding update to the specific force is, therefore, given by

$$\mathbf{y} = \tilde{\mathbf{a}}^i - (\tilde{\ddot{\mathbf{x}}}^i - \bar{\boldsymbol{\gamma}}^i) \tag{10}$$

where $\bar{\boldsymbol{\gamma}}^i$ denotes normal gravitation in the i-frame (normal gravity less the centrifugal acceleration due to the Earth's rotation). From Eqs. (2), (3), and (4), we also have

$$\mathbf{y} = C_b^i \mathbf{b}_a + C_b^i \mathrm{diag}(\tilde{\mathbf{a}}^b)\boldsymbol{\kappa}_a + \tilde{\mathbf{a}}^i \times \boldsymbol{\Psi}^i + C_b^i \boldsymbol{\varepsilon}_a - \delta\ddot{\mathbf{x}}^i - \delta\mathbf{g}^i \tag{11}$$

where

$$\delta\mathbf{g}^i = \mathbf{g}^i - \bar{\boldsymbol{\gamma}}^i \tag{12}$$

is the gravity disturbance vector using the usual convention in geodesy (which, however, is the negative of the error in gravity with respect to normal gravity). Note that the first equation, Eq. (10), consists of actual observed (calculated) and sensed quantities (GPS and INS accelerations); while the second equation, Eq. (11), is a model of this update in terms of the error parameters of the system.

Also note that the gravity disturbance vector, $\delta\mathbf{g}^i$, is not specifically included as a state of the system. Including it for estimation would require the interpretation of $\delta\mathbf{g}^i$ as a stochastic process, as well as a corresponding mathematical model for the process. In fact, many studies have been devoted to the development of such models, but it is not easy to achieve an accurate representation (even if the stochastic interpretation is valid). A gravity disturbance component along a given trajectory is neither a variable of a finite-order state-space nor does it satisfy a linear differential equation, as pointed out by Jekeli (1994) and Jordan (1972). The gravity disturbance vector is for now intentionally excluded from the observation model, thus reflecting an imposed premise that we have no prior information on its existence, as far as the system model is concerned. The consequence of this will actually allow us to find a kind of estimate for $\delta\mathbf{g}^i$.

In matrix form the *observation model* is expressed therefore as

$$\mathbf{y} + \delta\mathbf{g}^i = H\mathbf{s} + \mathbf{v} \tag{13}$$

where the observation matrix and observation noise vector are given, respectively, by

$$H = \begin{bmatrix} C_b^i & 0 & C_b^i \mathrm{diag}(\tilde{\mathbf{a}}^b) & 0 & [\tilde{\mathbf{a}}^i\times] \end{bmatrix} \tag{14}$$

$$\mathbf{v} = C_b^i \boldsymbol{\varepsilon}_a - \delta\ddot{\mathbf{x}}^i \tag{15}$$

and where $[\tilde{\mathbf{a}}^i\times]$ is a skew-symmetric matrix with elements arranged to emulate the cross-product. Assuming $\boldsymbol{\varepsilon}_a$ and $\boldsymbol{\varepsilon}_G$ are uncorrelated, $\mathbf{v} \sim \mathrm{N}\ (\mathbf{0}, C_b^i D_a C_i^b + D_G)$.

On the basis of the system dynamics, Eq. (9), and the updates, Eq. (10), the state vector, $\mathbf{s}$, can be estimated using the usual Kalman filter formulation (Brown and Hwang 1992). If the estimated parameters are denoted $\hat{\mathbf{s}}$, then the *adjusted* observations are given by

$$\hat{\mathbf{y}} = H\hat{\mathbf{s}} \tag{16}$$

The residual of the adjusted observation relative to the *observed value*, Eq. (10), is given by

$$\begin{aligned} \boldsymbol{\upsilon} &= \mathbf{y} - \hat{\mathbf{y}} \\ &= -\delta\mathbf{g}^i + C_b^i(\delta\mathbf{b}_a + \mathrm{diag}(\tilde{\mathbf{a}}^b)\delta\boldsymbol{\kappa}_a) \\ &\quad - \tilde{\mathbf{a}}^i \times \delta\boldsymbol{\Psi}^i + C_b^i\boldsymbol{\varepsilon}_a - \boldsymbol{\varepsilon}_G \end{aligned} \tag{17}$$

where $\delta\mathbf{s} = \left(\delta\mathbf{b}_a^{\mathrm{T}} \quad \delta\mathbf{b}_g^{\mathrm{T}} \quad \delta\boldsymbol{\kappa}_a^{\mathrm{T}} \quad \delta\boldsymbol{\kappa}_g^{\mathrm{T}} \quad (\delta\boldsymbol{\Psi}^i)^{\mathrm{T}}\right)^{\mathrm{T}}$ is the true error in the estimates

$$\delta\mathbf{s} = \hat{\mathbf{s}} - \mathbf{s} \tag{18}$$

The residual is computed using Eq. (10) but, as seen in Eq. (17), it contains the gravity disturbance vector as well as the true errors in the estimates of the system parameters and the noise of the inertial sensors and the observed kinematic acceleration (the gyro errors enter through $\delta\boldsymbol{\Psi}^i$). If we can assume that the latter errors are all small compared to the gravity disturbance vector, then the (negative) residual is an estimate of it

$$\boldsymbol{\upsilon} \approx -\delta\mathbf{g}^i \tag{19}$$

This method of determining the gravity disturbance vector, while simultaneously estimating the sensor errors, is based on the customary technique of detecting outliers in a least-squares (LS) adjustment by inspecting the residuals corresponding to the adjusted observations. Significant systematic behavior in the residuals usually implies faulty or deficient modeling. Of course, serious caveats must accompany this method. The spectral components of the gravity disturbance signal that (when transformed into the time domain by the vehicle's velocity) exhibit the same characteristics as the sensor errors will be absorbed by the corresponding estimates in the Kalman filter. This means that the true errors in the estimates, $\delta\mathbf{s}$, can be large and thus may vitiate the result of Eq. (19). In essence, the feasibility of the method depends on the separability of the gravity disturbance signal from the effects of sensor errors on the acceleration; this is also the case with any other approach.

It may now be argued that having discovered a flaw in the model (as indicated by the presumably systematic behavior of the residuals), the model must be changed to include the gravity disturbance vector as an error parameter to be estimated. This approach is studied after first investigating the residuals with actual test data. Aside from this gravity modeling issue, we may contrast the present method for estimating the gravity disturbance vector with the more traditional approach based on GPS position updates (Jekeli 1994) as follows.

(1) The former is expressed entirely in terms of accelerations, not positions. Ultimately we seek the gravity vector, and this formulation is conceptually

easier, more straightforward, and computationally less expensive since the complicated inertial navigation equations do not have to be integrated.

(2) The calculations are performed in the *i*-frame instead of the navigation frame (*n*-frame, or local-level frame), which is defined by the directions of local north, east, and down. This also simplifies the formulations and thus improves the computational efficiency.

(3) The total gravity vector is determined, not just its horizontal components. This is possible since no free-inertial navigation solution is computed (which is not feasible in the vertical direction).

3 Test data

The data used in this study were collected by the University of Calgary on 1 June 1995 and made available by the Special Study Group 3.164 of the International Association of Geodesy. They include the coordinates of an airborne GPS antenna at 0.5-s intervals, and raw accelerometer and gyro data at a data rate of 50 Hz. The purpose of this airborne gravity survey over the Canadian Rocky Mountains was to assess repeatability as well as the accuracy of airborne gravimetry using GPS and INS. The airborne system consisted of a strapdown inertial system, the Honeywell LASEREF III, and two GPS receivers, the Ashtech Z-XII and the NovAtel GPSCard. In order to perform differential GPS (DGPS) positioning, three base stations were also operated on the ground.

In this survey, four flights were carried out, all east–west approximately over the same ground track. The total length of the profile was 250 km and the flying altitude was around 5.5 km above mean sea level. The terrain elevation varied from 500 to 3000 m with approximate mean of 1500 m. Average flying speed was approximately 430 km/h, so the corresponding spectral resolution for 90 and 120 s smoothing is approximately 5.0 to 7.0 km. For details on the data description see Wei and Schwarz (1998).

Figure 1 shows the trajectories of three of the four flights. Legs 1 and 3 are almost on top of each other and Leg 2 is about 0.005 degrees ($\approx$ 540 m) to the north.

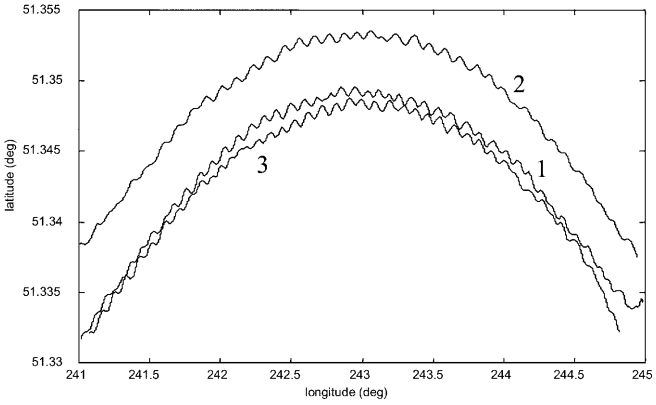

Fig. 1. Three flight trajectories for the test data of June 1995

Note the strong oscillations characterizing the dynamics of the flight. The principal oscillations occurred around the first (along-track) and the third (vertical, down) axes of the body frame, corresponding to roll and yaw rotations. These dynamics were probably caused by the auto-pilot function of the airplane which automatically maintains the direction and the velocity of the airplane. A plot of the attitude of the airplane (Fig. 2) for one of the lines shows that the roll and yaw motions have an amplitude of about 2.5° and a period of about 55 s.

It may already be guessed that separating the gravity signal with frequencies in the range of these dynamics will be difficult. The effect of the dynamics will be explained in more detail later.

4 Data processing

Four main procedures are involved in the new technique (Fig. 3). First, the GPS accelerations are derived from the GPS positions, calculated with the DGPS technique, by applying a numerical differentiator. A fifth-order B-spline differentiator was applied to the GPS positions to obtain these kinematic accelerations. Since the numerical differentiation tends to amplify high-frequency components, the accelerations were smoothed to reduce these high frequency noises. For this purpose, a third-order B-spline smoother with a window length of 60 s

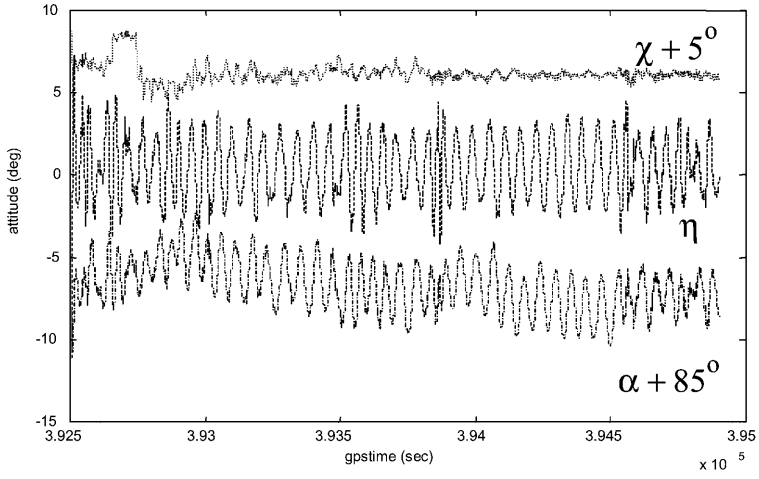

Fig. 2. The attitude of the airplane for Line 1 (392 500–394 900 GPS seconds), χ = pitch, η = roll, α = roll

was applied to the raw GPS accelerations. This 60-s smoothing was shown to be enough to yield GPS acceleration better than 1 mGal accuracy (Jekeli and Garcia 1997). The B-spline smoother was used because of its elegant theory and model behavior in numerical calculations (Kincaid and Cheney 1996).

Second, the raw INS data (increments of velocities and angles) are integrated to generate the *b*-frame inertial measurement unit (IMU) accelerations. A third-order Runge–Kutta integration algorithm, using quaternions, was applied for this procedure (Jekeli 2000). For consistency, the IMU acceleration was also averaged by the same third-order B-spline smoother applied to GPS acceleration.

Third, Kalman filtering is performed to estimate the INS system errors. Here, the GPS acceleration is used as an update value and the residuals from the filter are assumed to approximate the gravity disturbance vector. These residuals were found to retain significant non-gravitational systematic errors. Therefore, in a final step, biases and trends were removed with the assumption of known endpoint values. In addition, the residuals from the three legs were processed with a wavenumber correlation filter (WCF) to remove remaining systematic errors. The WCF, developed by von Frese et al. (1997), decomposes space domain data into wave domain coefficients through a Fourier transformation, and then constructs the correlation spectrum by comparing coefficients of a pair of co-registered data at the corresponding wavelength.

The wavenumber correlation coefficient between two data sets **x** and **y** is defined as

$$CC_k = \cos(\Delta\theta_k) = \frac{x_k \cdot y_k}{|x_k||y_k|} \tag{20}$$

where CC_k is the correlation coefficient for the wavenumber $k, \Delta\theta_k$ is the phase difference of the data sets **x** and **y**, $\Delta\theta_k = \theta_{\bar{x}} - \theta_{\bar{y}}$, and $\cdot$ denotes the scalar product of vectors. Based on the above wavenumber correlation coefficient, the components showing less correlation than a certain tolerance are assumed as noise and filtered out.

The repeated tracks of the test data provide an opportunity to decorrelate the gravity signal from some of the systematic errors, since we can assume that the gravity signal is commonly detected in all three legs, while the random noise and systematic errors should not be common. Using the WCF, long-term trends as well as medium-frequency airplane dynamic effects, can be removed to some extent.

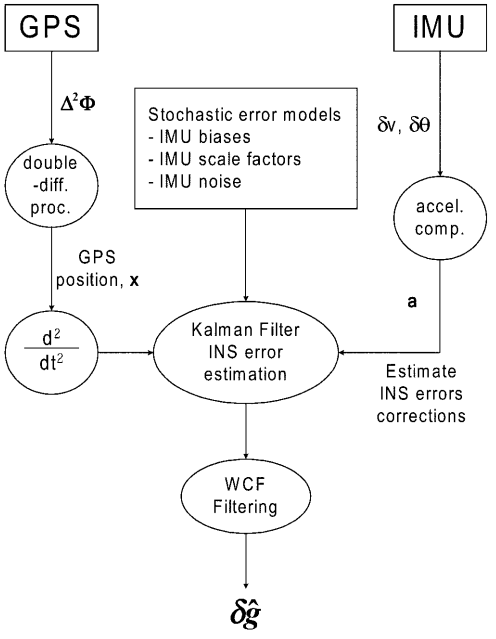

Fig. 3. Schematic diagram for acceleration update algorithm

5 Results and analysis

Figure 4 shows the difference between the GPS and INS accelerations, after taking out the normal gravitation, i.e. Eq. (10), but rotated into the *n*-frame. Note that the means are removed for clarity in the plots. In an ideal situation, this should be the gravity disturbance vector according to Eqs. (1), (10), and (12). However, the results still contain systematic errors, especially large trends, in all components. Note that the overall trend in Leg 2 is opposite to that in Legs 1 and 3 for the north components. In addition, strong high-frequency oscillations appear in the north component. Because the airplane mainly flew in the east–west direction, the roll motions of the vehicle directly affect the acceleration of the north component. These high-frequency oscillations are a consequence of the dynamics of the aircraft, also called *phugoid* motion (Boedecker and Neumayer 1995).

As we can see, the simple difference between the GPS and INS acceleration already shows the gravitational signature. In particular, the down component is very

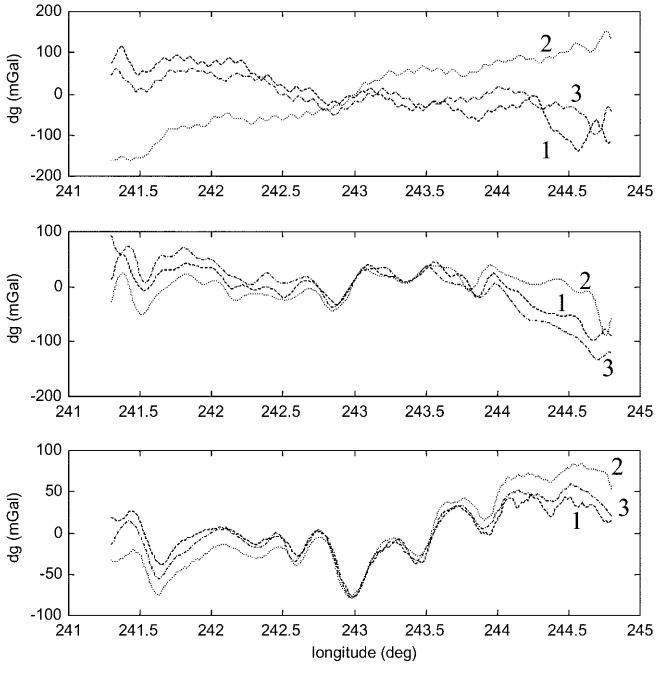

Fig. 4. Difference between the smoothed GPS and INS accelerations [Eq. (10)] in the *n*-frame, with means removed, for Legs 1, 2 and 3; north (*top*), east (*middle*), and down (*bottom*)

well detected; for example, look at the low anomaly around 393 700 GPS seconds and the high anomaly around 393 300. Since the down component is not much affected by the orientation errors, it does not include a significant trend.

A numerical comparison against control data provided by the National Imagery and Mapping Agency (NIMA) (for the deflections of the vertical) and by the University of Calgary (for the down component) is shown in Table 1. The accuracy of the control data is estimated to be better than 5 and 1.3 mGal for the horizontal and down components, respectively. In should be noted that the horizontal control data are different from those presented in Jekeli and Kwon (1999), where EGM96 was inadvertently omitted.

The large standard deviations for the horizontal components (18–78 mGal) are caused mostly by the trends due to the orientation error, as seen in Fig. 4. As expected, the down component shows much better standard deviation than the horizontal components. In particular, for Leg 3 it has the very good accuracy of 4.5 mGal.

Next, it is attempted to estimate the orientation and sensor errors through the Kalman filter developed in Sect. 2. Only the accelerometer bias and orientation errors are included in the unknown parameter vector in this study. Because the effects of the scale factor errors appear mainly in the high-frequency components, it is assumed that these are essentially removed in the smoothing procedure. Furthermore, the high correlation between the orientation error and gyro bias hinders the separation between them, and the result would not be improved by including both as system states. The initial values are set to zero, and the initial variances are set to 20 mGal, 2 arc seconds, and 2 arc minutes, respectively, for accelerometer biases, horizontal and vertical orientation errors.

The residuals from the Kalman filter are shown in Figs. 5–7. In general, the results are much improved compared to the observations themselves (Fig. 4). The large biases have mostly vanished. Almost all high/low anomalies are detected in all three legs, and the trends in the north and down components are significantly reduced through the filter. The east components, however, still contain large errors at both ends of the profiles in all three lines. In addition, the high-frequency oscillations remain in the north direction. This makes sense, because these oscillations cannot be removed by estimating the low-frequency parameters such as orientation errors and biases. Numerical comparison with respect to the control data shows tremendous improvement in north and down components (Table 2). The minimum and maximum standard deviations with respect to the control data occur in the down component of Leg 3 (3.9 mGal)

Table 1. Means and standard deviations (mGal) of observations (GPS acceleration–INS acceleration–normal gravity) with respect to control data

		Leg 1	Leg 2	Leg 3
North	SD	63.4	77.9	35.3
	Mean	−272.9	−573.9	−827.2
East	SD	31.1	18.6	46.67
	Mean	−108.5	−16.8	−215.9
Down	SD	10.9	12.4	4.5
	Mean	35.4	96.8	131.3

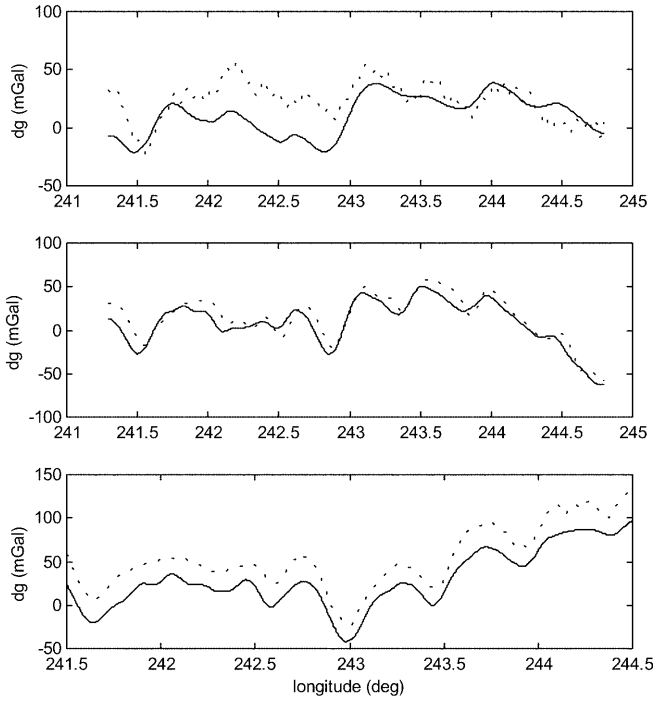

Fig. 5. Residuals from Kalman filter (*dashed*) and control data (*solid*) for north (*top*), east (*middle*), and down (*bottom*) component for Leg 1

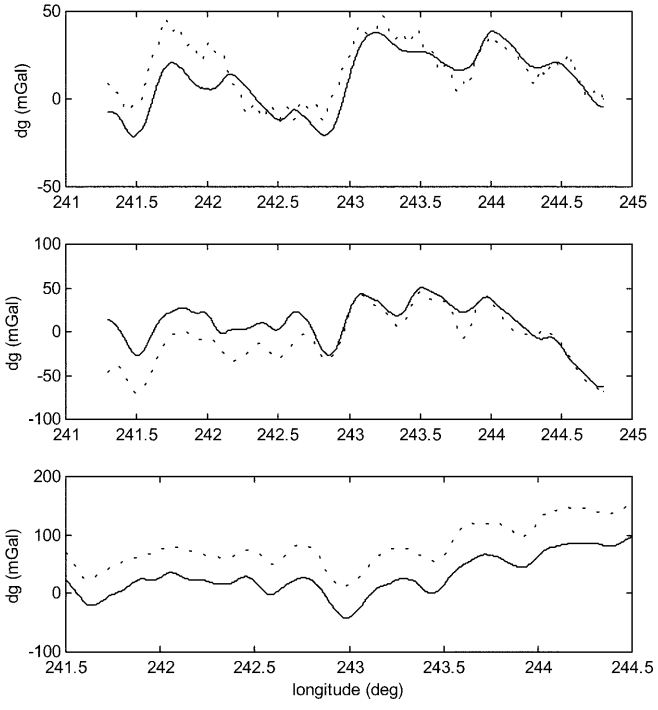

Fig. 6. Residuals from Kalman filter (*dashed*) and control data (*solid*) for north (*top*), east (*middle*), and down (*bottom*) component for Leg 2

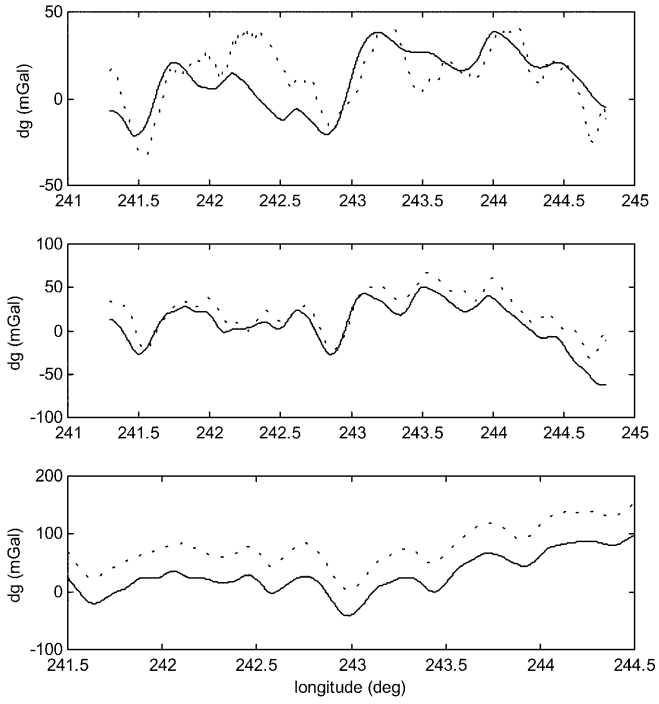

Fig. 7. Residuals from Kalman filter (*dashed*) and control data (*solid*) for north (*top*), east (*middle*) and down (*bottom*) component for Leg 3

Table 2. Means and standard deviations (mGal) of residuals from the Kalman filter with respect to control data

		Leg 1	Leg 2	Leg 3
North	SD	17.5	10.1	15.3
	Mean	−12.6	−5.7	−2.5
East	SD	8.6	14.9	10.8
	Mean	−6.2	16.5	−13.3
Down	SD	5.0	6.5	3.9
	Mean	25.0	52.4	49.0

and the north component of Leg 1 (17.5 mGal), respectively.

That systematic sensor errors are not completely removed from the residuals is reasonable, as seen in Eq. (17). Since the system is basically a relative measurement system, the biases between the residuals and the control data cannot be determined unless a gravity value at a point is available. In order to eliminate the biases and some additional long-term uncompensated systematic errors in the residuals, an endmatching, linear correction is applied using the known gravity disturbance vector at the ends of the profile.

Table 3 shows the means and the standard deviations of the residuals with respect to the control data after applying the endmatching procedure. As expected, the east component in Leg 3 significantly improves, while the others slightly improve or deteriorate.

As explained previously, the WCF is very efficient in extracting a signal from co-registered data. Therefore, as a final procedure in refining the residual from the Kalman filter, the WCF was applied to all combinations of

Table 3. Means and standard deviations (mGal) of the difference between residuals, after endmatching, and control data

		Leg 1	Leg 2	Leg 3
North	SD	14.4	8.6	14.3
	Mean	11.8	4.6	6.2
East	SD	8.7	9.1	10.4
	Mean	4.3	−16.3	22.5
Down	SD	5.1	5.0	3.5
	Mean	−8.7	2.2	−2.0

two parallel tracks (Leg 1–2, Leg 1–3, and Leg 2–3). The results from the WCF show significant improvements in combinations Leg 1–2 and Leg 2–3. However, the Leg 1–3 combination does not show any improvement (see Figs. 8–10).

This illustrates a very interesting feature, namely, the dependency of the INS errors on the direction of the flight. Leg 1 and 3 are in the same direction, so the characteristics of the long-term INS errors are almost the same, while for Leg 2 they have opposite characteristics. Therefore, remaining long-term errors in oppositely traveled paths are canceled through the WCF as in the Leg 1–2 and Leg 2–3 combinations. WCF applied to the combination Leg 1–3, however, does not remove the errors because they have common characteristics. Numerical comparison with the control data after applying the WCF is given in Table 4.

The best standard deviation for the down component (3.2 mGal) is obtained for the Leg 2–3 combination. The other two combinations also show that the down

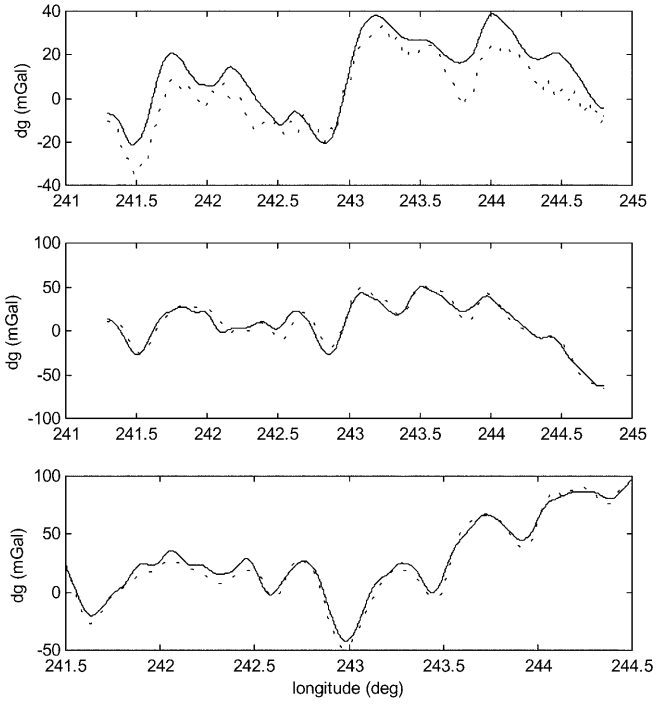

Fig. 8. Residual after endmatching and WCF vs control data for Leg 1–2 combination

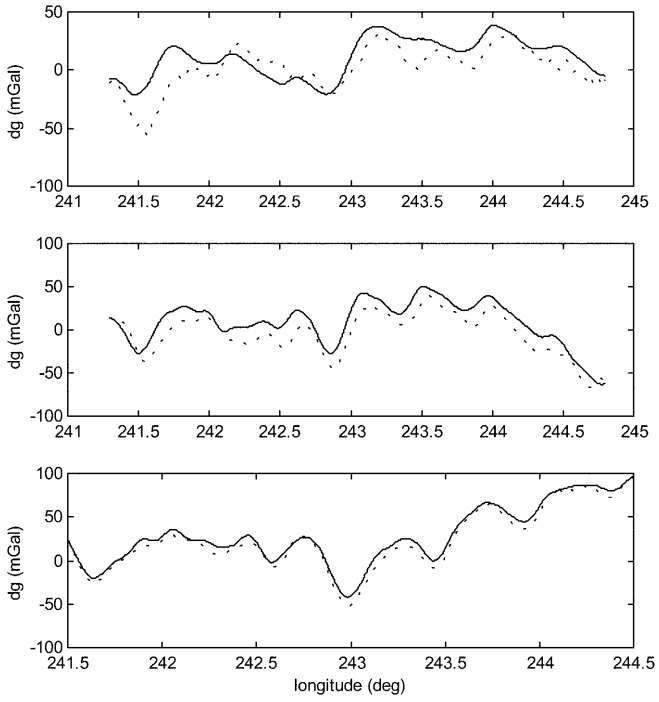

Fig. 9. Residual after endmatching and WCF vs control data for Leg 1–3 combination

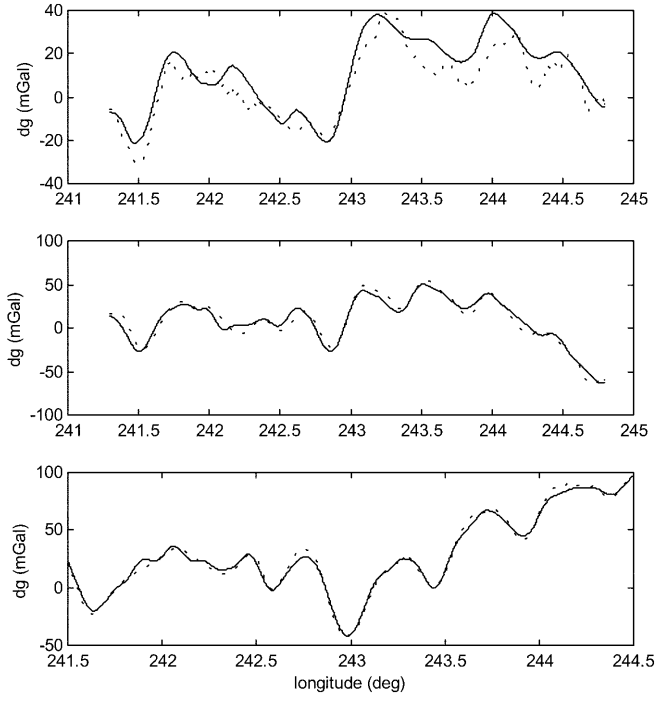

Fig. 10. Residual after endmatching and WCF vs control data for Leg 2–3 combination

component can be recovered with an accuracy of 3–4 mGal. Although not as good as the vertical component, the horizontal components have very good accuracies (5.8–6.2 mGal). Therefore, it can be concluded that the deflection of vertical can be recovered with an accuracy better than 1.3 arc seconds (1 arc second $\approx$ 4.75 mGal).

Table 4. Means and standard deviations (mGal) of the difference between residuals, after endmatching and WCF, and control data

		Leg 12	Leg 13	Leg 23
North	SD	5.8	12.7	5.9
	Mean	8.2	9.0	5.4
East	SD	6.2	8.4	6.1
	Mean	−0.3	13.4	−0.3
Down	SD	4.3	3.4	3.2
	Mean	−3.2	−5.3	0.1

6 Discussions

Although the results from the new algorithm compared well with the control data, there are disadvantages. One is that it yields no standard deviations for the estimated gravity disturbances because they are not really estimated as system states. This implies that the method is theoretically incomplete, and the rigorous solution would be to include a gravity model into the system dynamics. However we can always integrate a gravity model in the new approach by augmenting Eq. (9). Toward this objective, two gravity models were designed and tested. The first model selected for each gravity disturbance component was the well-known third-order Gauss–Markov model (Gelb 1994). The number of parameters increases to 24 by adding nine parameters for the gravity disturbances, and the design matrix, H, and the dynamic matrix, F, have to be properly expanded

$$\underset{3\times 24}{H} = \left[C_b^i \;\; 0 \;\; C_b^i \mathrm{diag}(\tilde{\mathbf{a}}^b) \;\; 0 \;\; [\tilde{\mathbf{a}}^i\times] \;\; I \;\; 0 \;\; 0\right] \tag{21}$$

$$\underset{24\times 1}{\mathbf{s}} = \left[\mathbf{b}_a^{\mathrm{T}} \;\; \mathbf{b}_g^{\mathrm{T}} \;\; \boldsymbol{\kappa}_a^{\mathrm{T}} \;\; \boldsymbol{\kappa}_g^{\mathrm{T}} \;\; \boldsymbol{\Psi}^{\mathrm{T}} \;\; (\delta\mathbf{g}^i)^{\mathrm{T}} \;\; (\delta\mathbf{g}')^{\mathrm{T}} \;\; (\delta\mathbf{g}'')^{\mathrm{T}}\right]^{\mathrm{T}} \tag{22}$$

$$F = \begin{bmatrix} F_{11} & 0 \\ 0 & F_{22} \end{bmatrix} \tag{23}$$

where F_{11} is given by F in Eq. (9) and

$$F_{22} = \begin{bmatrix} 0 & 0 & 0 & 1 & 0 & 0 & 0 & 0 & 0 \\ 0 & 0 & 0 & 0 & 1 & 0 & 0 & 0 & 0 \\ 0 & 0 & 0 & 0 & 0 & 1 & 0 & 0 & 0 \\ 0 & 0 & 0 & 0 & 0 & 0 & 1 & 0 & 0 \\ 0 & 0 & 0 & 0 & 0 & 0 & 0 & 1 & 0 \\ 0 & 0 & 0 & 0 & 0 & 0 & 0 & 0 & 1 \\ -\beta_1^3 & 0 & 0 & -3\beta_1^2 & 0 & 0 & -3\beta_1 & 0 & 0 \\ 0 & -\beta_2^3 & 0 & 0 & -3\beta_2^2 & 0 & 0 & -3\beta_2 & 0 \\ 0 & 0 & -\beta_3^3 & 0 & 0 & -3\beta_3^2 & 0 & 0 & -3\beta_3 \end{bmatrix} \tag{24}$$

and $\delta\mathbf{g}'$, $\delta\mathbf{g}''$ represent auxiliary parameters that transform the third-order differential equations for the Gauss–Markov process to first order. β_1, β_2, and β_3 are the corresponding correlation parameters of the processes. The initial values for the accelerometer biases and orientation errors are the same as for the no-gravity

model case. The scale factor errors and gyro biases are not estimated for the reasons stated in the previous section. Various values for these parameters and for the variances of the gravity models were tested. Of these, one of the best results with a correlation distance of about 12 km and variance of 900 mGal^2 is presented in Fig. 11 for all three legs.

The estimates of all three gravity disturbance components are poorer than the residuals based on the no-gravity model, as seen by comparing Fig. 11 to Figs. 5, 6, and 7. Overall, the standard deviations of the horizontal components, as well as of the vertical component, are several times larger (Table 5). In particular, the east component of Leg 1 shows the worst result (Standard deviation = 58.3 mGal), caused by the instability of the filter at the beginning of the trajectory. The best result was obtained for the down component of Leg 3, with a standard deviation of 7 mGal.

The second type of gravity model selected is rather empirical, composed of trigonometric functions. Since the residual from the original approach seems to reflect largely the gravity disturbance, a frequency analysis is performed on the residual. After identifying the principal frequency band, or highest frequency component, supposedly contained in the gravity signature, these disturbances are modeled as combinations of trigonometric functions with limited frequency bands in the time or spatial domain, where the amplitudes are parameters to be estimated. In other words, each gravity disturbance component is modeled as

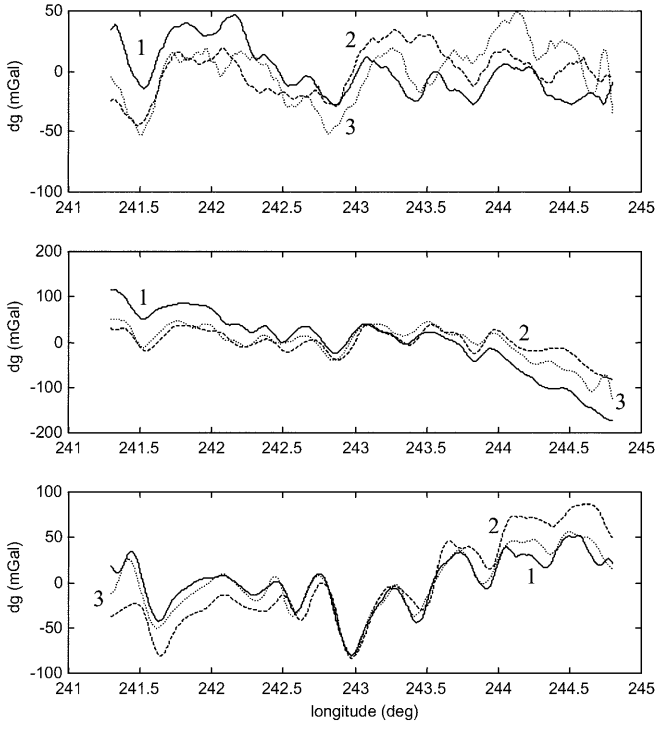

Fig. 11. Estimated gravity disturbances modeled by a third-order Gauss–Markov process for Legs 1, 2 and 3; north (*top*), east (*middle*), and down (*bottom*)

Table 5. Standard deviations of difference between estimated gravity disturbances modeled by third-order Gauss–Markov process and control data (mGal)

	Leg 1	Leg 2	Leg 3
North	26.3	9.0	14.7
East	58.3	15.5	23.4
Down	12.5	13.9	7.0

$$\begin{aligned}\delta g_i &= \sum_{k=0}^{n} a_{jk}\cos\frac{2\pi kt}{T} + \sum_{k=0}^{n} b_{jk}\sin\frac{2\pi kt}{T}\\ &= a_{j0} + a_{j1}\cos\frac{2\pi t}{T} + a_{j2}\cos\frac{2\pi\cdot 2t}{T} + \cdots\\ &\quad + a_{jn}\cos\frac{2\pi\cdot nt}{T} + b_{j1}\sin\frac{2\pi t}{T} + b_{j2}\sin\frac{2\pi\cdot 2t}{T} + \cdots\\ &\quad + b_{jn}\sin\frac{2\pi\cdot nt}{T}\\ &= D_j\cdot\boldsymbol{\beta}_j \end{aligned} \tag{25}$$

The matrix D_j consists of trigonometric functions dependent on time, t. The vector $\boldsymbol{\beta}_j$ consists of the coefficients of the trigonometric functions. With all three components combined, we have

$$\delta\mathbf{g} = D\cdot\boldsymbol{\beta} \tag{26}$$

where

$$\underset{3\times 3(2n+1)}{\mathbf{D}} = \begin{bmatrix} D_1 & 0 & 0\\ 0 & D_2 & 0\\ 0 & 0 & D_3\end{bmatrix}$$

$$\begin{aligned}\underset{1\times(2n+1)}{D_1} &= D_2 = D_3\\ &= \left[1\cos\frac{2\pi t}{T}\cos\frac{2\pi t\cdot 2}{T}\cdots\sin\frac{2\pi t}{T}\right.\\ &\quad \left.\times\sin\frac{2\pi t\cdot 2}{T}\cdots\sin\frac{2\pi t\cdot n}{T}\right]\end{aligned}$$

$$\underset{3(2n+1)\times 1}{\boldsymbol{\beta}} = \begin{bmatrix}\boldsymbol{\beta}_1\\ \boldsymbol{\beta}_2\\ \boldsymbol{\beta}_3\end{bmatrix}$$

$$\boldsymbol{\beta}_1 = \begin{bmatrix} a_{10}\\ a_{11}\\ a_{12}\\ \vdots\\ a_{1n}\\ b_{11}\\ \vdots\\ b_{1n}\end{bmatrix},\quad \boldsymbol{\beta}_2 = \begin{bmatrix} a_{20}\\ a_{21}\\ a_{22}\\ \vdots\\ a_{2n}\\ b_{21}\\ \vdots\\ b_{2n}\end{bmatrix},\quad \boldsymbol{\beta}_3 = \begin{bmatrix} a_{30}\\ a_{31}\\ a_{32}\\ \vdots\\ a_{3n}\\ b_{31}\\ \vdots\\ b_{3n}\end{bmatrix} \tag{27}$$

With maximum order of expansion n, the number of unknown parameters increases by $3\times(2n+1)$; the sizes of the design matrix H, state vector $\mathbf{s}$, and the dynamics

matrix F, should be expanded accordingly. The coefficients of the trigonometric functions are modeled as random constants with initial variance of 1 m/sec^2. We have

$$\underset{3\times(15+6n+3)}{H} = \left[C_b^i \;\; 0 \;\; C_b^i \mathrm{diag}(\tilde{\mathbf{a}}^b) \;\; 0 \;\; [\tilde{\mathbf{a}}^i\times] \;\; D\right] \tag{28}$$

$$\underset{(15+6n+3)\times 1}{\mathbf{s}} = \left[\mathbf{b}_a^{\mathrm{T}} \;\; \mathbf{b}_g^{\mathrm{T}} \;\; \boldsymbol{\kappa}_a^{\mathrm{T}} \;\; \boldsymbol{\kappa}_g^{\mathrm{T}} \;\; \boldsymbol{\Psi}^{\mathrm{T}} \;\; \boldsymbol{\beta}_1^{\mathrm{T}} \;\; \boldsymbol{\beta}_2^{\mathrm{T}} \;\; \boldsymbol{\beta}_3^{\mathrm{T}}\right]^{\mathrm{T}} \tag{29}$$

$$\underset{(15+6n+3)\times(15+6n+3)}{F} = \begin{bmatrix} F_{11} & 0 \\ 0 & \underset{(6n+3)\times(6n+3)}{0} \end{bmatrix} \tag{30}$$

Clearly, we have to decide the maximum order n of the trigonometric expansion. Higher order would generate more detail in the gravity disturbance signal, but would require much more calculation time. In order to decide the maximum order for the expansion, a simple LS fit of the residual could be performed. In this study, it was shown that n should be at least 20 to obtain 2 mGal accuracy of fit to the residuals. The actual estimation was done with $n = 10$, which already required a very long computation time.

Figure 12 shows the resulting estimates of the gravity disturbance components for all three legs. These estimates appear much smoother than the residuals with no gravity modeling (Figs. 5–7). Furthermore, the high-frequency oscillations in the north component residuals

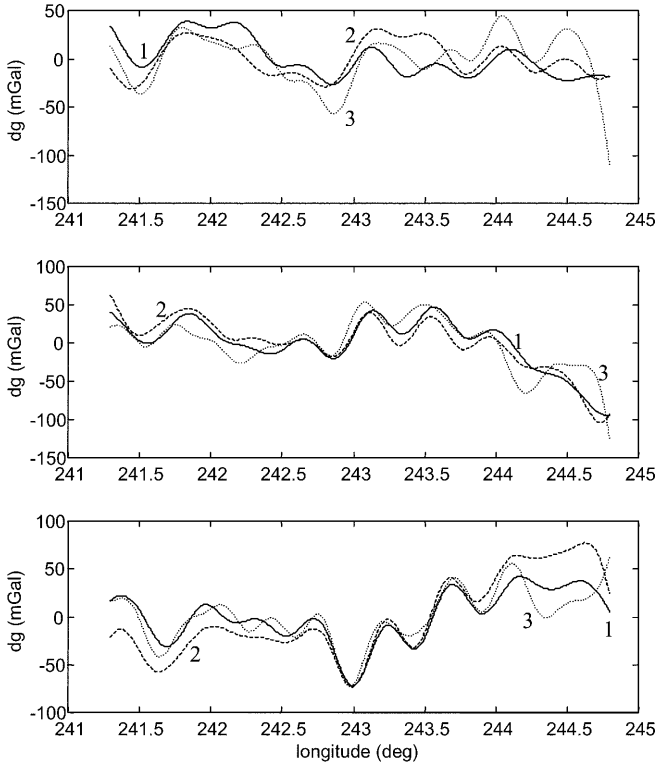

Fig. 12. Estimated gravity disturbances modeled by trigonometric expansions of order 10 for Legs 1, 2 and 3; north (*top*), east (*middle*), and down (*bottom*)

Table 6. Standard deviations of differences between estimated gravity disturbances modeled by trigonometric expansions and control data (mGal)

	Leg 1	Leg 2	Leg 3
North	24.1	12.5	18.0
East	16.6	22.0	21.7
Down	12.6	9.4	16.4

are absent in this case because of the low-frequency modeling.

Numerically the results are more consistent among the legs and more stable than in the case of Gauss–Markov modeling (Table 6). However, they are still worse than for the case of the no-gravity model. The maximum standard deviation appears in the north component of Leg 1 (24.1 mGal) and the minimum occurs in the down component of Leg 2 (9.4 mGal).

It is expected that better estimates could be obtained with higher-order expansions, as well as with careful selection of the frequency band in this approach. Since the purpose of this test was not to design a gravity model but to show a modification of the mathematical model for theoretical completeness, further refinement to improve the results was not pursued.

7 Conclusion

This research addressed a new efficient algorithm for recovery of the vector gravity field from data collected by GPS and INS. The new algorithm has three distinct features compared to the traditional algorithm. First, accelerations from GPS are used as updates in the new algorithm while positions are used in the traditional approach. Second, the gravity disturbance vector is not modeled stochastically in the new approach. The 'estimated' gravity disturbance is identified with the residual from a Kalman filter estimation of the sensor error parameters. Third, the frame selected for all calculations is the inertial frame, while the navigation frame is selected in the traditional approach.

Application to real data, however, showed that this residual cannot fully separate the orientation error from the horizontal gravity disturbances. In addition, the residual also contains the effect of system white noise. Therefore, further data processing, comprising endpoint matching and WCF, was applied to the residuals to extract a more refined gravity disturbance signal. The final results from all processing show that accuracies of approximately 6 and 3–4 mGal can be achieved for the horizontal and vertical components, respectively. The result for the vertical component is comparable to that of other investigators (Wei and Schwarz 1998); for the horizontal component, the results demonstrate a new capability.

There are several lessons to be learned from this study. First, aircraft dynamics greatly influence horizontal gravity component estimation, as seen in the

north component of the INS acceleration. Second, the endpoint data are important to eliminate residual trends and biases. Third, multiple traverses over the same gravity signal are important to reduce other systematic errors, e.g. by using the waveform correlation filter. The tracks may be spaced apart by a distance equal to the resolution of the recovered signal.

For theoretical completeness, two types of gravity models, Gauss–Markov processes and trigonometric expansions, were included in the system dynamics and tested. In both cases, the gravity estimates were worse than the no-gravity model residuals when compared to the control data. This emphasizes the known difficulty in stochastically modeling the gravity disturbance; based on these tests, it is not a recommended approach. The approach with the trigonometric expansion showed less dependency on the a priori information, and better estimates are expected if we include higher-order terms and carefully select the frequency band. However, the calculations then become extremely expensive and better numerical algorithms or computing systems will be required.

Acknowledgement. This research is supported by the National Imagery and Mapping Agency (NIMA), Contract No. NMA202-98-1-1110.

References

Boedecker G, Neumayer H (1995) An efficient way to airborne gravimetry: integration of strapdown accelerometer and GPS-system performance in selected frequency bands in a dynamic environment. Proc IAG Symposium on Airborne Gravity Field Determination, IUGG XXI General Assembly, Boulder, 2–14 July, pp 23–28

Brown RG, Hwang PYC (1992) Introduction to random signals and applied Kalman filtering. John Wiley, New York

Brozena JM (1991) GPS and airborne gravimetry: recent progress and future plans. Bull Geod 65: 116–121

Brozena JM, Peters MF (1994) Airborne gravity measurement at NRL. Proc Int Symp Kinematic Systems in Geodesy, Geomatics and Navigation, Banff, 30 August–2 September, pp 495–506

Eissfeller B, Spietz P (1989) Basic filter concepts for the integration of GPS and an inertial ring laser gyro strapdown system. Manuscr Geod 14: 166–182

Forsberg R (1987) A new covariance model, for inertial gravimetry and gradiometry. J Geophys Res 92(B2): 1305–1310

Forsberg R, Kenyon S (1994) Evaluation and downward continuation of airborne gravity data – the Greenland example. Proc Int Symp Kinematic Systems in Geodesy, Geomatics, and Navigation (KIS 94), pp 531–538

Gelb A (1994) Applied optimal estimation. MIT Press, Cambridge, MA

Glennie C, Schwarz KP, Bruton AM, Forsberg R, Olesen AV, Keller K (2000) A comparison of stable platform and strapdown airborne gravity. J Geod 74: 383–389

Grejner-Brzezinska DA, Wang J (1998) Gravity modeling for high-accuracy GPS/INS integration. Navigation 45: 209–220

Hein GW (1995) Progress in airborne gravimetry: solved, open and critical problems. Proc IAG Symp Airborne Gravity Field Determination, IUGG XXI General Assembly Boulder, 2–14 July, pp 3–11

Jekeli C (1992) Vector gravimetry using GPS in free-fall and in an earth-fixed frame. Bull Geod 66: 54–61

Jekeli C (1994) Airborne vector gravimetry using precise, position-aided inertial measurement units. Bull Geod 69: 1–11

Jekeli C (1995) GPS/INS positioning and the earth's gravitational field. Proc 1995 Mobile Mapping Symp, The Ohio State University, Columbus, 24–26 May, pp 163–172

Jekeli C (1998) An analysis of vertical deflections derived from high-degree spherical harmonic models. J Geod 73: 10–22

Jekeli C (2000) Inertial navigation systems with geodetic applications. Walter deGruyter, Berlin

Jekeli C, Garcia R (1997) GPS phase accelerations for moving-base vector gravimetry, J Geod 71: 630–639

Jekeli C, Kwon JH (1999) Results of airborne vector (3-D) gravimetry. Geophys Res Lett 26: 3533–3536

Jordan SK (1972) Self-consistent statistical models for the gravity anomaly, vertical deflections, and undulation of the geoid. J Geophys Res 77(20): 3660–3670

Kincaid D, Cheney W (1996) Numerical analysis. Brooks/Cole, Pacific Grove, CA

Knickmeyer ET (1990) Vector gravimetry by combination of inertial and GPS satellite measurements. Rep 20035, Department of Surveying Engineering, The University of Calgary

Lemoine FG, Kenyon SC, Factor JK, Trimmer RG, Palvis NK, Chinn DS, Cox CM, Klosko SM, Luthcke SB, Torrence MH, Wang YM, Williamson RG, Palvis EC, Rapp RH, Olson TR (1998) The development of the joint NASA GSFC and the National Imagery and Mapping Agency (NIMA) geopotential model EGM96, NASA/TP, 1998-206861. Goddard Space Flight Center, Greenbelt, MD

Salychev OS, Bykovsky AV, Voronov VV, Schwarz KP, Liu Z, Wei M, Panenka J (1994) Determination of gravity and deflections of the vertical for geophysical applications using the ITC-2 platform. Proc Int Symp Kinematic Systems in Geodesy, Geomatics and Navigation, Banff, 30 August–2 September, pp 521–529

Tapley B, Watkins M, Ries J, Davis G, Eanes R, Poole S, Rim H, Schutz B, Shum C, Nerem R, Lerch F, Marshall J, Klosko S, Pavlis N, Williamson R (1996) The joint gravity model 3. J Geophys Res 101(B12): 28 029–28 049

von Frese RB, Jones MB, Kim JW, Kim JH (1997) Analysis of anomaly correlations. Geophysics 62(1): 342–351

Wang J (1998) Stochastic model versus deterministic model in INS/GPS positioning, ISPRS, Commission III Symp, 6–10 July, Columbus

Wei M, Schwarz KP (1998) Flight test results from a strapdown airborne gravity system. J Geod 72(6): 323–332